17 (2025) 100532

Contents lists available at ScienceDirect

Carbon Capture Science & Technology

journal homepage: www.elsevier.com/locate/ccst

Full Length Article

Electroreduction of CO_2 to C1 and C2 products on dual active sites

Naimat Ullah [a], Munzir H. Suliman [a], Sikandar Khan [b,c], Zubair Ahmed Laghari [d], Guillermo Diaz-Sainz [e], Abdulmajeed Hendi [a,f], Wan Zaireen Nisa Yahya [d], Muhammad Usman [a,*]

[a] Interdisciplinary Research Center for Hydrogen Technologies and Carbon Management (IRC-HTCM), King Fahd University of Petroleum & Minerals (KFUPM), Dhahran 31261, Saudi Arabia
[b] Department of Mechanical Engineering, King Fahd University of Petroleum & Minerals (KFUPM), Dhahran 31261, Saudi Arabia
[c] Interdisciplinary Research Center for Intelligent Manufacturing and Robotics (IRC-IMR), King Fahd University of Petroleum & Minerals (KFUPM), Dhahran 31261, Saudi Arabia
[d] Department of Chemical Engineering, Centre of Research in Ionic Liquids, Universiti Teknologi PETRONAS, Seri Iskandar 32610, Perak, Malaysia
[e] Departamento de Ingenierías Química y Biomolecular, Universidad de Cantabria, Avenida de los Castros s/n, 39005 Santander, Spain
[f] Physics Department, King Fahd University of Petroleum & Minerals (KFUPM), Dhahran 31261, Saudi Arabia

ARTICLE INFO

Keywords:
eCO_2RR
CuS-ZnS catalysts
Flow cell
Affordable and clean energy
Climate action

ABSTRACT

Electrochemical CO_2 reduction (eCO_2RR) is a promising method for transforming CO_2 emissions into useful multicarbon products. This study involved the synthesis and evaluation of CuS/ZnS nanocomposites with varying compositions (CuS: ZnS = 1:1, 2:1, and 1:2) in both H-type and flow-cell electrolyzers. The catalyst with a 2:1 CuS/ZnS ratio (S2) exhibited excellent performance, with a Faradaic efficiency (FE) of 60 % for C_1 products and approximately 20 % for C_2 products (C_2H_4) at a current density of -280 mA·cm^{-2} in the flow-cell configuration. The flow-cell arrangement significantly enhanced catalytic activity, suppressed hydrogen evolution, and increased selectivity for CH_4 and C_2H_4 at greater negative potentials. Augmented ethylene production was ascribed to Cu-rich active sites promoting efficient C–C coupling and increased CO_2 accessibility at gas diffusion electrodes (GDEs), corroborated by low charge-transfer resistance (~1 Ω·cm^2). This work emphasizes the pivotal importance of catalyst composition and reactor design, showcasing the 2:1 CuS/ZnS catalyst in a flow-cell format as a scalable and effective method for sustainable CO_2 conversion to multicarbon fuels. Density functional theory (DFT) calculations further validated the experimental results by revealing favorable adsorption energies and interactions between the CuS/ZnS catalyst and key intermediates in the CO_2 conversion process.

Introduction

Carbon dioxide (CO_2) emissions have surged in recent decades due to industrialization. The release of CO_2 into the environment through the combustion of fossil fuels for power generation has caused significant global environmental concerns such as global warming, sea level rise, land degradation, and other ecological impacts (Patel and Mehta, 2023; Usman et al., 2025b; Usman et al., 2022). The conversion of CO_2 into valuable chemical commodities i.e., C_1 and energy-intensive C_2 compounds, via chemical processes has emerged as a promising approach for CO_2 reutilization. These conversions can be achieved through various photochemical, electrochemical, photo-electrochemical, or biochemical processes.

Among these,eCO_2RR has attracted considerable research interest due to (a) precise control of operating conditions such as potential and temperature, (b) adoptability to diverse reaction conditions including organic or aqueous electrolytes, and (c) scalability to industrial-scale operations. Besides, eCO_2RR can operate using renewable energy sources like solar or wind power, enabling efficient energy storage and redistribution while fostering sustainable energy solutions (Doğan et al., 2023; Huang et al., 2023; Usman et al., 2025a).

According to literature and ongoing research advances, eCO_2RR catalysts are broadly classified into metal-based and metal-free categories based on product selectivity, synthesis, and design. Metal-based electrocatalysts include bare metals and their hybrid compositions, such as metal alloys, metal oxides, metal sulfides, and metal complexes. The activity and selectivity of these electrocatalysts vary significantly depending on metal employed, primarily due to differences in catalytic

* Corresponding author.
E-mail address: muhammadu@kfupm.edu.sa (M. Usman).

https://doi.org/10.1016/j.ccst.2025.100532
Received 7 August 2025; Received in revised form 16 October 2025; Accepted 17 October 2025
Available online 17 October 2025

activity and adsorption strength of reaction intermediates (Mukherjee et al., 2024; Wei et al., 2023; Abdinejad et al., 2019).

Despite notable progress, several challenges hinder the industrial applicability of eCO_2RR (Kong et al., 2023). These include: (1) high overpotential, as CO_2 is a thermally stable, chemically inert and linear molecule; (2) sluggish kinetics of complex proton-coupled electron transfer processes and poor CO_2 solubility of in aqueous media, limiting electron transfer rates; and (3) low exchange current densities, which reduce overall catalytic efficiency (Yan et al., 2023; Ullah et al., 2025). Most CO_2 electrocatalysts reported to date operate at very low current densities, far below those of commercial electrolyzers that achieve efficiencies exceeding 70 % at current densities above 200 mA cm^2. Additionally, challenges include (1) poor product selectivity requiring costly separations, (2) catalyst deactivation within 100 h, which limits practical industrial application and scale-up, and (3) competition from the hydrogen evolution reaction (HER), which dominates at higher overpotentials due to favorable energy conditions, resulting in a higher faradaic yield of H_2 relative to desired eCO_2RR products. Recently, substantial efforts have been devoted to designing and synthesizing innovative, cost-effective and durable electrocatalysts to overcome these limitations and enable efficient large-scale CO_2 reduction at lower overpotentials (Zhang et al., 2023a; Ding et al., 2023). Electrochemical CO_2 reduction can also be steered toward tunable syngas (H_2/CO). Recent Cu-based studies show alloying on Cu mesh enables composition control of syngas (Luo et al., 2024) while Cu–Zn bimetallic tune CO/H_2 ratios by adjusting Zn loading and balancing eCO_2RR vs. HER, (Guo et al., 2025) in parallel, metal–N–C catalysts deliver near-quantitative syngas with ratio control by potential (Zhao et al., 2020).

Copper (Cu) is electrochemically capable of converting CO_2 into energy-dense C_2+ products, garnering significant attention. However, the formation of C–C bonds necessary to yield C_2+ products requires overcoming a high activation energy barrier, leading to poor activity and selectivity. Thus, synthesizing Cu electrocatalysts optimized to overcome this energy barrier is critical for advancing eCO_2RR (Nitopi et al., 2019; Li et al., 2023; Yang et al., 2023; Suliman et al., 2025; Suliman et al., 2022). The activity and selectivity of Cu depend on particle size and crystal facet; for example, Cu(111) favors methane production, whereas Cu(100) promotes C_2 products. Meanwhile, Single-atom Cu and nanoparticles demonstrate higher efficiency and current density compared to bulk Cu (Hori et al., 2003). Copper-based electrocatalysts have been extensively studied for their ability to facilitate C–C coupling for multicarbon product synthesis. However, pure Cu suffers from low FE and poor selectivity due to the interference from the competing HER. Bimetallic Cu-based electrocatalysts improve both the selectivity and overall performance of copper (Suliman et al., 2025; Chen et al., 2024; Suliman et al., 2024). Burdyny's group reported a 93 % faradaic efficiency with a current density o 150 mA cm^2 for formate production using Cu–Pd within a zero-gap flow cell running at −2.9 V vs RHE (Abdinejad et al., 2023). Bimetallic Ag-Cu catalysts also enhance CO_2 electroreduction efficiency and selectivity; a 10 wt. % Ag-Cu complex achieved 70 % faradaic efficiency for C_2 products, comprising 40 % ethanol and 30 % ethylene at −1.0 RHE in a flow cell, significantly outperforming Ag-free catalysts.

Copper sulfide-based nanomaterials have recently gained interest as electrocatalysts due to their p-type semiconducting properties, availability, and non-toxicity. Various copper sulfide phases have been reported in the literature (Suliman et al., 2025; Khan et al., 2022). Metal electrodes such as Au, Ag, Zn, Cu, and their alloys have also been widely explored for CO_2 reduction to CO, but are limited by low current densities and high overpotential. More recently, transition metal sulfides have garnered interest due to their catalytic activity. Surface modification via sulfur infiltration is a well-documented process that enhances adhesion corrosion resistance, and provides a low-cost method to form thin transition metal sulfides layers. This study aims to employ sulfur infiltration to enhance CO_2 reduction efficiency (Zhang et al., 2020; Yan et al., 2024).

Zinc sulfide (ZnS) is widely used in electrochemistry due to its chemical resistance, non-toxicity, and low cost. However, its potential for CO_2 electro-reduction remains largely unexplored (Zhen et al., 2019). ZnS is also known to stabilize CO_2-based intermediates, enhancing selectivity towards CO and other oxygenated products. When combined with CuS, ZnS contributes synergistically, with CuS promoting C–C coupling process and ZnS controlling intermediate adsorption and reaction kinetics (Song et al., 2021; Mosali et al., 2024).

In this work, the concept of dual active sites refers to the cooperative roles of the CuS and ZnS domains within the heterostructured catalyst. Cu-rich sites promote CO adsorption and C–C coupling, which are essential for generating C_2 products such as ethylene, while Zn-related sites stabilize OCHO intermediates, favoring C_1 products such as formate. The presence of sulfur contributes additional functionality by modifying the electronic structure, enhancing conductivity, and stabilizing active Cu^+ species, thereby supporting efficient CO_2 reduction pathways. Thus, the intimate CuS/ZnS interfacial contact provides two distinct yet synergistic catalytic centers in a sulfur-rich matrix, enhancing both activity and selectivity during eCO_2RR. Similar dual-site mechanisms at Cu–Zn–S interfaces have been reported to improve reaction kinetics and product distribution by tuning intermediate adsorption energies (Juntrapirom et al., 2021; Jia et al., 2023; Zhang et al., 2023b). In this study, CuS/ZnS nanocomposites with varied CuS: ZnS ratios (1:1, 2:1, and 1:2) are synthesized and characterized to evaluate their activity for electrochemical CO_2 reduction using H-cell and flow cell setups. The influence of catalyst composition and mass transport on product selectivity will be assessed. Faradaic efficiency and product yields will be investigated, focusing on conditions that promote C_2 product formation without compromising long-term catalytic stability for practical scale-up. Understanding the synergistic interactions between ZnS and CuS at different ratios will provide insights for designing scalable, cost-effective catalysts for efficient CO_2 conversion using sustainable processes. Unlocking these interactions is key to developing next-generation electrocatalysts with improved selectivity and durability for real-world CO_2 utilization applications. To further complement the experimental findings,DFT calculations were performed to reveal molecular-level interactions and adsorption energies between the CuS/ZnS catalyst and key reaction intermediates, thereby validating and strengthening the observed catalytic performance.

Experimental section

Materials

Copper sulfate pentahydrate ($CuSO_4{\cdot}5H_2O$, 99.95 %), sodium sulfide nonahydrate ($Na_2S{\cdot}9H_2O$,98 %), and zinc acetate (99 %) were purchased from Sigma-Aldrich (USA). Ethanol (C_2H_5OH,99.8 %), methanol (99 %), and dimethylformamide (C_3H_7NO,99.9 %) were procured from Sharlu (Sharjah, UAE).

Synthesis of CuS

The synthesis of CuS nanoparticles involved a wet chemical process. The process began by dissolving 1.5 g of $CuSO_4{\cdot}5H_2O$ in 25 mL of deionized water, followed by stirring the resulting solution at 60 °C for 30 min to ensure full dissolution of the copper sulfate. In a separate container, 0.8 g of $Na_2S{\cdot}9H_2O$ was dissolved in 50 mL of DI water with continuous stirring to form a homogeneous sodium sulfide solution. The sodium sulfide solution was then added slowly to the copper sulfate solution under constant stirring at 60 °C. A black precipitate formed immediately, indicating the formation of CuS. The mixture was stirred for an additional 3 h to ensure complete reaction, followed by 6 h of stirring to promote nanoparticle growth. After completion, the black precipitate was collected by centrifugation and washed thoroughly with DI water, followed by ethanol to remove any impurities. Finally, the precipitate was dried in an oven at 120 °C for 24 h.

Synthesis of CuS/ZnS nanocomposite

Co-precipitation was used for the synthesis of CuS/ZnS nanocomposites. Dimethylformamide (DMF) and deionized water were used as solvents, with zinc acetate and sodium sulfide serving as zinc and sulfur sources, respectively. The synthesis began by dispersing a known quantity of pre-synthesized CuS in 40 mL of DMF, followed by sonication for 30 min and continuous stirring for 1 h. A known quantity of zinc acetate was then added to this solution. To achieve a 1:1 molar ratio of ZnS to CuS, an equimolar amount of $Na_2S{\cdot}9H_2O$ was dissolved in 40 mL of DI water. This sodium sulfide solution was slowly added to the zinc acetate-DMF solution under constant stirring (Fig. 1a). Stirring was continued for 3 h until the solution became clear. The mixture was then left undisturbed at room temperature for 24 h to complete the reaction. The resulting precipitate was collected by centrifugation and washed with DI water and methanol. The product was dried in an oven at 100 °C for 24 h. Catalysts are named by composition as CuS:ZnS(a:b), where a and b are the molar parts of CuS and ZnS, respectively; samples formerly labeled S1, S2, and S3 are now CuS:ZnS(1:1), CuS:ZnS(2:1), and CuS:ZnS (1:2), used consistently throughout.

Electrode preparation

A catalyst ink was prepared by mixing 10 mg of catalyst with 1 mL of a solvent mixture containing 750 μL of ethanol, 200 μL of DI water, and 50 μL of 5 % Nafion solution. The mixture was sonicated for 10 min to ensure uniform dispersion. Then, 50 μL of the ink suspension was carefully drop-cast onto 1.0 cm^2 piece of conductive carbon paper and left to dry at room temperature.

Preparation of electrode for H-type of cell

The CO_2 reduction reaction was first evaluated using an H-cell system, which consisted of a silver-silver chloride (Ag/AgCl) reference electrode and a platinum mesh counter electrode. The catalyst-coated conductive carbon paper (Fig. 1b) served as the working electrode.

Electrolyte pH plays a decisive role in steering CO_2 reduction pathways and product selectivity. In our study, the H-cell operated in 0.5 M $KHCO_3$ (pH ≈ 7.4) provides a near-neutral environment with higher CO_2 solubility, through equilibrium with $KHCO_3$, which typically favors the formation of C_1 products (CO, HCOOH) but also allows the HER to remain highly competitive (Nitopi et al., 2019). Electrochemical reactions were controlled and monitored using a Gamry 620 potentiostat. Linear sweep voltammetry (LSV) was performed to determine overpotentials at various current densities. The measured current values were normalized to the electrode's geometric surface area (1 cm^2) for comparison. All potentials were converted to the reversible hydrogen electrode (RHE) scale using:

$$E_{RHE} = E_{Ag/AgCl} + 0.059 * pH + E^{\circ}_{Ag/AgCl}$$

Where $E^{\circ}_{Ag/AgCl} = 0.199$ V

Tafel slopes were calculated using the equation:

$$\eta = -A + log_{10} i/i_0$$

where η is the overpotential (V), i is the current density (A/m^2), i_o is the exchange current density (A/m^2) at η = 0, and A is a constant related to the Tafel slope (Suliman et al., 2024; Usman and Suliman, 2023).

Preparation of electrode for flow-cell

The working electrodes were fabricated using a spray-painting technique. A 100-microliter (μL) volume of the previously prepared ink was applied under controlled airflow and pressure to ensure uniform and consistent deposition onto the GDE using a spray gun.

The flow cell employed 1 M KOH (pH ≈ 14), where the abundance of OH^- ions suppress HER and creates a locally alkaline microenvironment that stabilizes *CO intermediates and facilitates C–C coupling, thereby promoting the production of multicarbon products such as C_2H_4 (Wang et al., 2019; Kas et al., 2016). Literature confirms that raising the electrolyte alkalinity not only enhances C_2 selectivity but also improves current densities by accelerating mass transport and lowering proton availability. The improved ethylene formation observed in our flow-cell experiments is therefore consistent with these findings, demonstrating that synergy between Cu-rich active sites and a highly alkaline medium is essential for boosting C–C coupling while minimizing HER (McGlynn et al., 2019; Dinh et al., 2018).

A flow cell was used to evaluate the performance at higher current densities. The eCO_2RR was carried out at varied potentials of −0.6 to −1.2 vs. RHE in 1-hour tests. After each test, liquid products were collected and analyzed using high-performance liquid chromatography (HPLC). Gaseous products were analyzed using gas chromatography with a barrier discharge ionization detector (GC-BID), which offers a sensitivity two orders of magnitude higher than that of traditional thermal conductivity detectors (TCD).

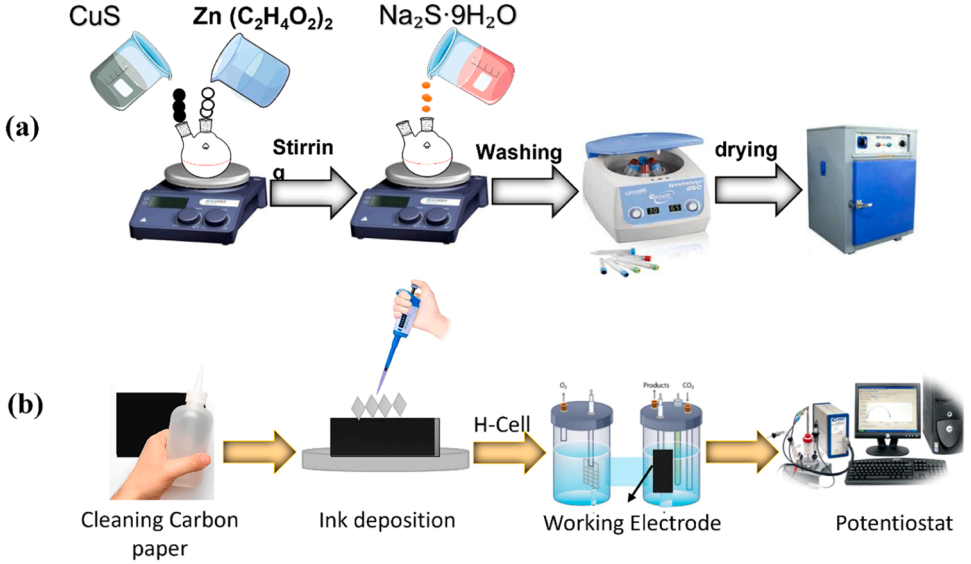

Fig. 1. **(a)** Flow chart for the synthesis of CuS/ZnS nanocomposite, and **(b)** Schematic representation of ink deposition on carbon paper for electrochemical analysis.

Electrochemical investigations and experiments

Cyclic voltammetry (CV) and LSV tests were conducted using in a 0.5 M potassium bicarbonate ($KHCO_3$) solution. The applied voltage ranged from 0.0 to −1.5 V vs. the reversible hydrogen electrode (RHE) (Usman and Suliman, 2023; Suliman et al., 2024).

$$Faradaic\ Efficiency\ (FE) = \frac{nZF}{Q} = \frac{nZF}{It} = \frac{nZF}{IV/v} * 100\%$$

where, n represents the amount of detected product (in moles, mol), while Q denotes the total charge passed through the system, recorded during electrolysis (in coulombs, C), F is the Faraday constant (96,485 C/mol), Z is the number of electrons transferred per molecule of product, I is the current (in amperes, A), t is the time needed to fill the sampling loop (in seconds, s), V represents the volume of the sampling loop (in cubic centimeters, cm^3), and *v* corresponds to the volume of the electrolyte (ml/s).

Electrochemical impedance spectroscopy (EIS) was performed over a frequency range from 10^5 to 0.1 Hz, maintaining consistent electrolyte and electrode conditions with those used in the LSV experiments.

Characterization techniques used

Powder X-ray diffraction (XRD) patterns of the samples were recorded using a Rigaku Mini Flex diffractometer equipped with Cu-Kα radiation. Data were collected over a 2θ range of 10° to 70° Surface morphology was examined using field-emission scanning electron microscopy (FESEM, LYRA 3 Dual Beam, Tescan) operating at 30 kV. FESEM samples were prepared by dispersing the materials in ethanol. Surface chemical analyses were conducted using X-ray photoelectron spectroscopy (XPS, ESCALAB 250Xi XPS Microprobe, Thermo Scientific, USA), equipped with an Al-Kα micro-focusing X-ray monochromator.

High-performance liquid chromatography analyses were conducted using an Agilent 12,400 Series HPLC System (Agilent Technologies) to quantify the compounds in the liquid samples. FESEM samples were prepared by dispersing the materials in ethanol. Electrochemical tests were carried out using a potentiostat (Gamry 620, Warminster, UK). Gas chromatography analyses were performed using a Shimadzu equipment (Nexis GC-2030). Field Emission Transmission Electron Microscope (FE-TEM) analysis was conducted using a JEM-2100F, a 200 kV FE microscope. Electrochemical Impedance Spectroscopy (EIS) measurements were carried out over a frequency range of 10^5 to 0.1 Hz, using the same electrolyte and electrode conditions as in the Linear Sweep Voltammetry (LSV) experiments.

This schematic (Fig. 2) highlights the critical interplay between intrinsic catalyst properties (composition, morphology, electronic structure, and active site density) and extrinsic operating factors (electrolyte, applied potential, cell design, and gas diffusion electrode) in determining the overall performance of eCO_2RR. The central flow-cell illustration represents the electrochemical environment where CO_2 molecules are converted on CuS/ZnS catalysts. By integrating catalyst design with reactor engineering, the figure emphasizes how this synergy governs the key outcomes of selectivity, activity, and stability. In particular, Cu-rich compositions in a flow-cell configuration enable efficient charge transfer and enhanced CO_2 accessibility, leading to high C_1 and C_2 product yields. Thus, the diagram conveys the central message of this work: efficient and sustainable CO_2 conversion is achieved only when intrinsic material properties are optimally aligned with extrinsic operational controls.

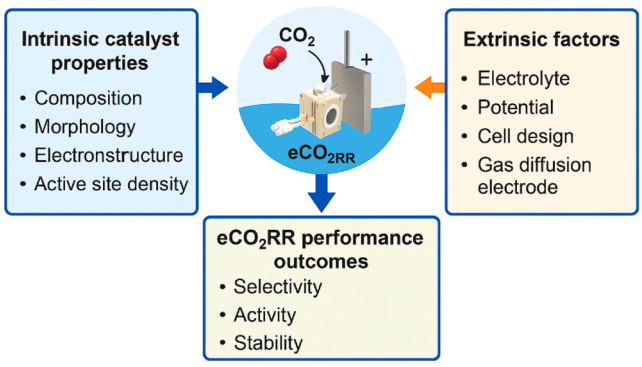

Fig. 2. Synergistic interaction of intrinsic catalyst properties and extrinsic factors governing eCO_2RR performance outcomes.

Computational set-up for density functional theory (DFT) calculations

To validate our experimental findings and identify the most favorable energy pathways, we computed the adsorption energies and analyzed the changes in bond alignment of the CuS–ZnS catalyst with various intermediates and adsorbates involved in the conversion of CO_2 to CO and HCOOH. These calculations were performed using the latest version of the CP2K-2025.2 package with the Quickstep module (Kühne et al., 2020). The Perdew-Burke-Ernzerhof (PBE) functional with Grimme's D3 van der Waals correction and Goedecker-Teter-Hutter (GTH) pseudopotential was employed during geometry optimization (Ramalho et al., 2013; Laghari et al., 2025). The TZV2P-MOLOPT-GTH for isolated molecules (adsorbates) was used, while the periodic structures of CuS and ZnS were optimized using DZVP-MOLOPT-SR-GTH basis set (Schütt and VandeVondele, 2018). A vacuum thickness of 15 Å was applied in the z-direction to avoid the interaction of molecules with boundary images. The lattice parameters of the constructed models were a = 7.535733 Å, b = 7.535733 Å, c = 34.361232 Å, and α=β=γ=90° as widely used in reported research work. The top two layers, which contain CuS and ZnS, were kept relaxed to maintain a 1:1 ratio for CuS and ZnS, whereas for the bottom layer, an additional atomic layer of ZnS, was kept fixed during geometry optimization. The vibrational analysis was performed using the same parameters to estimate the thermochemistry (i.e., entropy, enthalpy, zero-point energy, and Gibbs free energy) at standard temperature and pressure (STP). The Visual Molecular Dynamics (VMD) and Visualization for Electronic and Structural Analysis (VESTA) packages were used for visualization and molecular dynamics.

For the generation of eCO_2ER pathways, the computational Hydrogen Electrode (CHE) model was implemented using Gibbs free energy, which was calculated by adding the energies of the hydrogen molecule where needed, as stated in CHE model (Skúlason et al., 2010). The amount of hydrogen used was based on the number of electron-proton transfers. The Standard Hydrogen Electrode (SHE), in this dimension, is represented as given in the following equations.

$$H_2 \rightarrow 2H^+ + 2e^-$$

$$H^+\ (aq) + e^- \rightleftharpoons \tfrac{1}{2}H_2\ (g)$$

Following this approach, the free energies of all intermediates derived from DFT calculations, including Zero-Point-Energy (ZPE) were corrected, including the hydrogen reference energy (Skúlason et al., 2010).

The same computational methodology was applied to all adsorbates and intermediates involved in adsorption and activation processes on CuS/ZnS catalyst surface. The SHE was employed as a reference to compare catalytic sites and the species participating in CO_2 activation and subsequent CO and HCOOH desorption. For all reaction coordinates, the parameters used correspond to proton–electron transfer under standard conditions (pH = 7, 1 bar pressure, and 298 K temperature). The free energy of all systems was first optimized using DFT and subsequently used to construct free-energy profiles, while the adsorption energies (E_{ads}) were calculated using the following equation (Fields

et al., 2018):

$$E_{ads} = E_{catalyst+adsorbate} - E_{catalyst} - E_{adsorbate}$$

Where $E_{catalyst+adsorbate}$ is the energy of the complex structure where the adsorbate was adsorbed on the catalyst surface, $E_{catalyst}$ is the energy of the catalyst (CuS/ZnS) surface, and $E_{adsorbate}$ is the energy of the adsorbate.

Results and discussion

XRD analysis

The X-ray diffraction spectra (Fig. 3) of CuS, ZnS, and their composite materials (S1, S2, and S3) confirm the formation of crystalline CuS (covellite phase, JCPDS 06–0464) and ZnS (sphalerite phase, JCPDS 05–0566). In the composites, variations in peak intensity and broadening reflect the relative proportions of the two phases and the creation of CuS/ZnS heterostructures. Specifically, S2 (2:1 CuS/ZnS) displays more intense CuS-related peaks, whereas S3 (1:2 CuS/ZnS) is dominated by ZnS features. The observed shifts and changes in diffraction intensity indicate strong interfacial interactions, which are expected to influence the optoelectronic and catalytic properties of the composites. Using the Debye-Scherrer equation, the average crystallite sizes were determined to be 31 nm for CuS and 11 nm for ZnS. For the series samples, the sizes were 17, 21, and 13 nm for S1, S2, and S3, respectively (Jan et al., 2022). The XRD patterns of the catalysts before and after electrochemical analysis are shown in (supplementary information (SI),SI-Fig. 1.

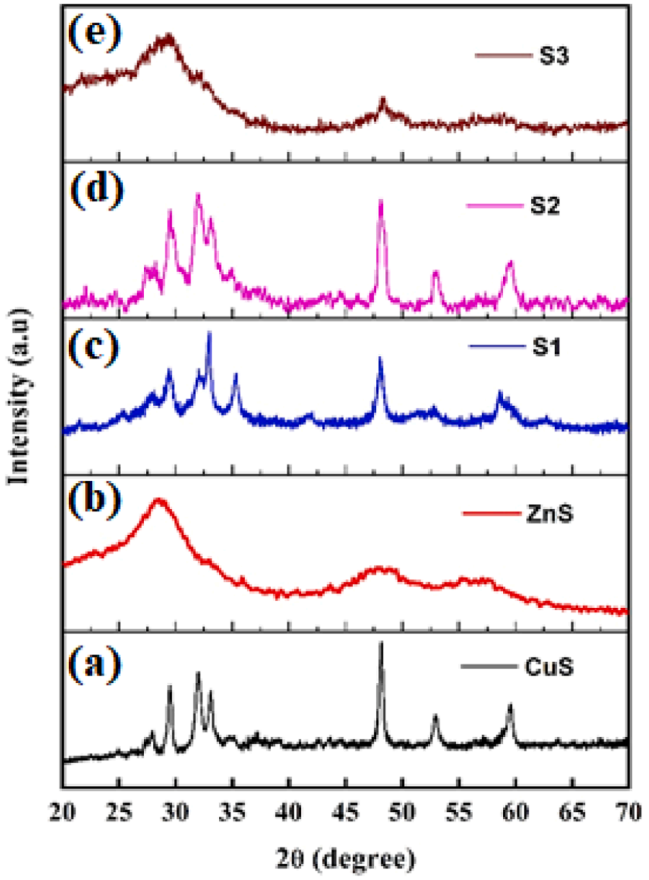

Fig. 3. XRD patterns of **(a)** CuS, (b)ZnS, **(c)** S1(1:1 CuS/ZnS), **(d)** (2:1 CuS/ZnS) and **(f)** (1:2 CuS/ZnS).

SEM, EXD analysis

The SEM images in Fig. 4 clearly illustrate the morphology of the CuS and the ZnS nanoparticles, as well as their nanocomposite. Fig. 4a shows the ZnS nanoparticles, which exhibit a porous and agglomerated structure indicative of a high surface area. The CuS nanoparticles (Fig. 4b) display a well-defined, plate-like crystalline morphology characteristic of covellite CuS, suggesting a well-controlled synthesis that likely enhances conductivity.

Fig. 4c presents the CuS/ZnS nanocomposite, where CuS (plate-like morphology) and ZnS (irregular spherical morphology) are integrated into a hybrid structure. The composite surface exhibits increased roughness and strong interfacial interactions, which contributed to enhanced charge transfer at the beginning of the section.

Figs. 3d and 3e display the EDX spectra of the CuS and CuS/ZnS samples, respectively Fig. 4d reveals prominent peaks for copper (Cu) and sulfur (S), confirming their presence in the CuS sample. Fig. 4e demonstrates the successful incorporation of zinc (Zn), alongsidecopper and sulfur in the CuS/ZnS composite, with no detectable impurities. These elemental peaks validate the formation, purity, and successful synthesis of the CuS/ZnS composite. The minor gold (Au) peak observed results from the gold coating applied to enhance conductivity during analysis.

TEM and elemental maping analysis

The TEM analysis of the CuS/ZnS composite is shown in Fig. 5(a–d), clearly highlighting its nanostructured morphology and crystallinity. The low-magnification TEM image in Fig. 5a shows aggregated nanoparticles with irregular shapes and uniform dispersion. A higher magnification image in Fig. 5b provides a closer view of the porous, interconnected nanostructures.

The high-resolution TEM (HRTEM) image in Fig. 5c confirms the crystalline nature of the composite, displaying distinct lattice fringes (detailed information in SI-Fig. 2) with interplanar spacings of 0.28 nm for the (103) plane of CuS and 0.31 nm for the (111) plane of ZnS, thereby validating the coexistence of both phases at the nanoscale.

The selected area electron diffraction (SAED) pattern in Fig. 5d shows sharp concentric rings with distinct spots, characteristic of the polycrystalline nature of the CuS/ZnS composite (Wang et al., 2016).

Elemental mapping (Fig. 5e-f) confirms the homogeneous distribution of copper (Cu), zinc (Zn), and sulfur (S) in both the CuS and CuS-ZnS composites. Copper and sulfur are uniformly distributed in CuS, while zinc is well incorporated into the CuS/ZnS composite, further confirming the material's homogeneity

XPS analysis

X-ray photoelectron spectroscopy (XPS) analysis (Fig. 6) confirmed the successful formation of the CuS/ZnS heterostructure. The survey spectrum clearly shows peaks corresponding to copper (Cu), zinc (Zn), sulfur (S), oxygen (O), and carbon (C), indicating the presence of these elements in the material.

In the high-resolution Cu 2p spectrum, the distinct Cu $2p_{3/2}$ and Cu $2p_{1/2}$ peaks, along with a characteristic satellite (shake-up) feature, indicate the presence of Cu^{2+} in CuS. From XPS atomic ratio calculations, the ratio between $Cu^{+}/Cu^{2+}$is around 1:2 as shown in SI (Table 1). The Zn 2p peaks around 1022 eV confirm the Zn^{2+} oxidation state, consistent with ZnS. in CuS/ZnS in S2p spectrum, two peaks at 161.2 and 162.5 eV corresponds to S 2p3/2 and p1/2 respectively. Meanwhile, another peaks were observed at 167.9 and 168.7 eV. This was recognized as S^{4+}, produced by the simultaneous coordination of the S to the Cu and Zn (Zhang et al., 2022). XPS confirms the presence of Cu^{2+} (Cu 2p with shake-up), Zn^{2+} (Zn 2p ~ 1022 eV), and S 2p components, supporting formation of a CuS (p-type)/ZnS (n-type) heterointerface

The observed O and C signals are attributed to surface-adsorbed

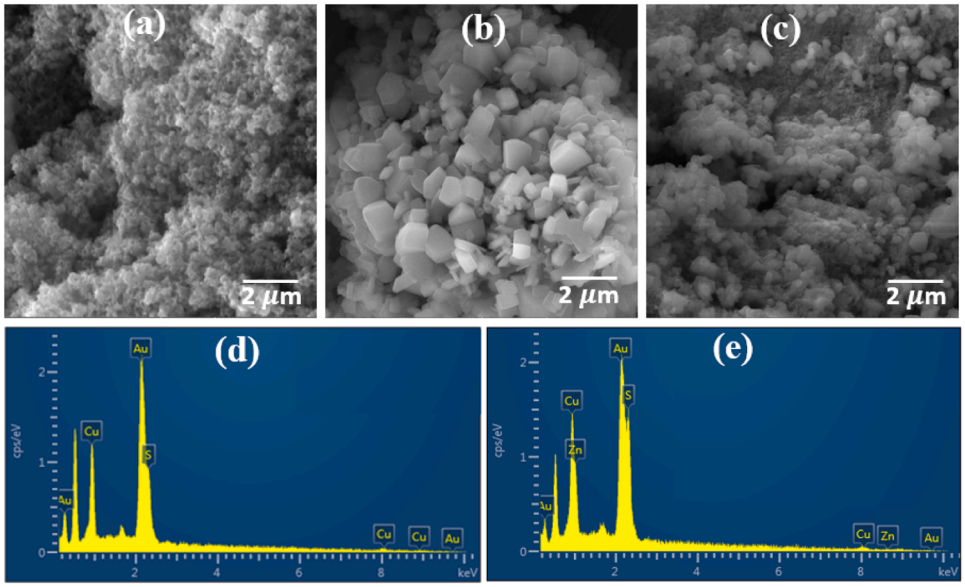

Fig. 4. SEM images of **(a)** ZnS, **(b)** CuS, **(c)** CuS/ZnS nanocomposite, and **(d)** EDX spectra of CuS **(e)** CuS/ZnS samples.

molecules or environmental contamination (Tang et al., 2024; Zhang et al., 2022; Stefan et al., 2016; Karikalan et al., 2017; VS and Mahesha, 2021; Suliman et al., 2024).

Electrochemical analysis and H-cell electrocatalytic evaluations

LSV was conducted to evaluate the electrochemical performance of CuS and ZnS/CuS composites with varying compositions (S1, S2, and S3). The polarization curves shown in Fig. 7a illustrate the catalytic activity of the electrodes in a CO_2-saturated electrolyte. The CuS electrode exhibits a current density of approximately 67 mA·cm^{-2}, indicating moderate electrocatalytic performance. Incorporation of ZnS into the composite significantly enhances the current density, reflecting improved charge transfer and catalytic efficiency. Among the composites, S2 (CuS/ZnS = 2:1) shows the highest current density at 130 mA·cm^{-2}, which is notably higher than S1 (83 mA·cm^{-2}) and S3 (96 mA·cm^{-2}). This enhancement is attributed to the optimal CuS/ZnS interface, which facilitates electron mobility of electrons and promotes electrochemical reactions. The improved current density suggests that the CuS-ZnS heterojunction increases active sites, enhances charge separation, and accelerates reaction kinetics.

Tafel analysis (Fig. 7b) reveals that the S2 electrocatalyst has the most favorable kinetics for CO_2 reduction, with a significantly lower Tafel slope of 63 mV/dec compared with CuS (342 mV/dec^{-2}), S1 (103 mV/dec^{-2}), and S3 (375 mV/dec^{-2}). This indicates that S2 requires a lower overpotential and has a reduced activation energy barrier for the reduction reaction, likely due to an enhanced electron transfer rate at the electrode-electrolyte interface (Wang et al., 2020; Zhou et al., 2022; Wang et al., 2024).

EIS was used to investigate the charge transfer kinetics at the electrode-electrolyte, with Nyquist plots displayed in Fig. 7c. The plots feature distinct semicircular arcs, where the diameter corresponds to the charge transfer resistance (Rct) associated with electrochemical reactions on the electrode surfaces. Smaller arc diameters indicate lower Rct and faster charge transfer kinetics. Approximate Rct values are 10 Ω cm^2 for CuS, 4 Ω cm^2 for S1, 1 Ω cm^2 for S2, and 4 Ω cm^2 for S3, demonstrating that the S2 electrode exhibits the most favorable charge transfer kinetics.

Electrochemical impedance spectra (Nyquist plots) were collected over 100 kHz–0.1 Hz and fitted using Gamry software with a Randles equivalent circuit. The fitted solution resistance (R_s) was ~3.8 Ω for all electrodes. After accounting for R_s, the charge-transfer resistances (Rct) are 1.8 Ω, 4.1 Ω, 4.3 Ω, and 6.1 Ω for electrodes S2, S1, S3, and CuS, respectively. Differences in R_{ct} reflect compositional and structural influences on charge transfer processes, which in turn affect the overall electrochemical performance (Lazanas and Prodromidis, 2023).

Double-layer capacitance (Cdl) measurements were conducted to estimate the electrochemically active surface area (ECSA) of the CuS and ZnS composite electrodes (Fig. 7d Cdl was determined from cyclic voltammograms acquired at 20, 50, 100, 150, and 200 mV s^{-1} by plotting capacitive current versus scan rate. S1 exhibits the highest Cdl (3.7 mF cm^{-2}), S2 is intermediate (1.5 mF cm^{-2}), and S3 the lowest (0.2 mF cm^{-2}), establishing ECSA: S1 > S2 > S3. Despite its smaller ECSA than S1, S2 delivers the best eCO_2RR performance and C_2 selectivity, indicating superior intrinsic site activity and interfacial chemistry that enhance *CO coverage and C–C coupling. Thus, ECSA alone does not dictate activity: S1's larger Cdl reflects more wetted area but not necessarily more active sites per area, whereas S2's lower Cdl (possibly from partial agglomeration/reduced wetted surface) is offset by higher-quality interfacial sites; the very low Cdl of S3 is consistent with the fewest accessible sites and correspondingly weaker response.

The higher current densiy of S2, together with its markedly lower Tafel slope (63 mV dec^{-1}) and smallest charge-transfer resistance (Rct ≈ 1 Ω cm^2), points to faster interfacial electron transfer at the CuS/ZnS junction; because S2 also shows the lowest Cdl among the series, these gains are attributed to improved intrinsic kinetics rather than a larger electrochemically active area.

Electroreduction of CO_2 was performed using catalysts CuS/ZnS with proportions S1 (1:1 CuS/ZnS), S2 (2:1 CuS/ZnS), and S3 (1:2 CuS/ZnS) in 0.5 M electrolyte of $KHCO_3$ using an H-cell. Chronoamperometry was conducted for 60 min, and gaseous and liquid products were analyzed via gas chromatography with GC-BID and UPLC, respectively

Fig. 8 presents the FE from H-cell tests for electrochemical CO_2 reduction using CuS/ZnS composites at different applied potentials (from –0.9 V to –1.5 V vs. RHE). Products analyzed include formic acid (HCOOH), ethylene (C_2H_4), methane (CH_4), carbon monoxide (CO), and hydrogen (H_2).

In Fig. 8a, the 1:1 CuS/ZnS composite shows a balanced product distribution across potentials, with CO and H_2 as dominant products. CO FE peaks at lower potentials and decreases at more negative potentials, while H_2 production increases, typical of enhanced proton reduction. Minor amounts of CH_4 and C_2H_4 indicate modest hydrocarbon formation at higher cathodic potentials.

Fig. 8b shows that the 2:1 CuS/ZnS sample exhibits significantly

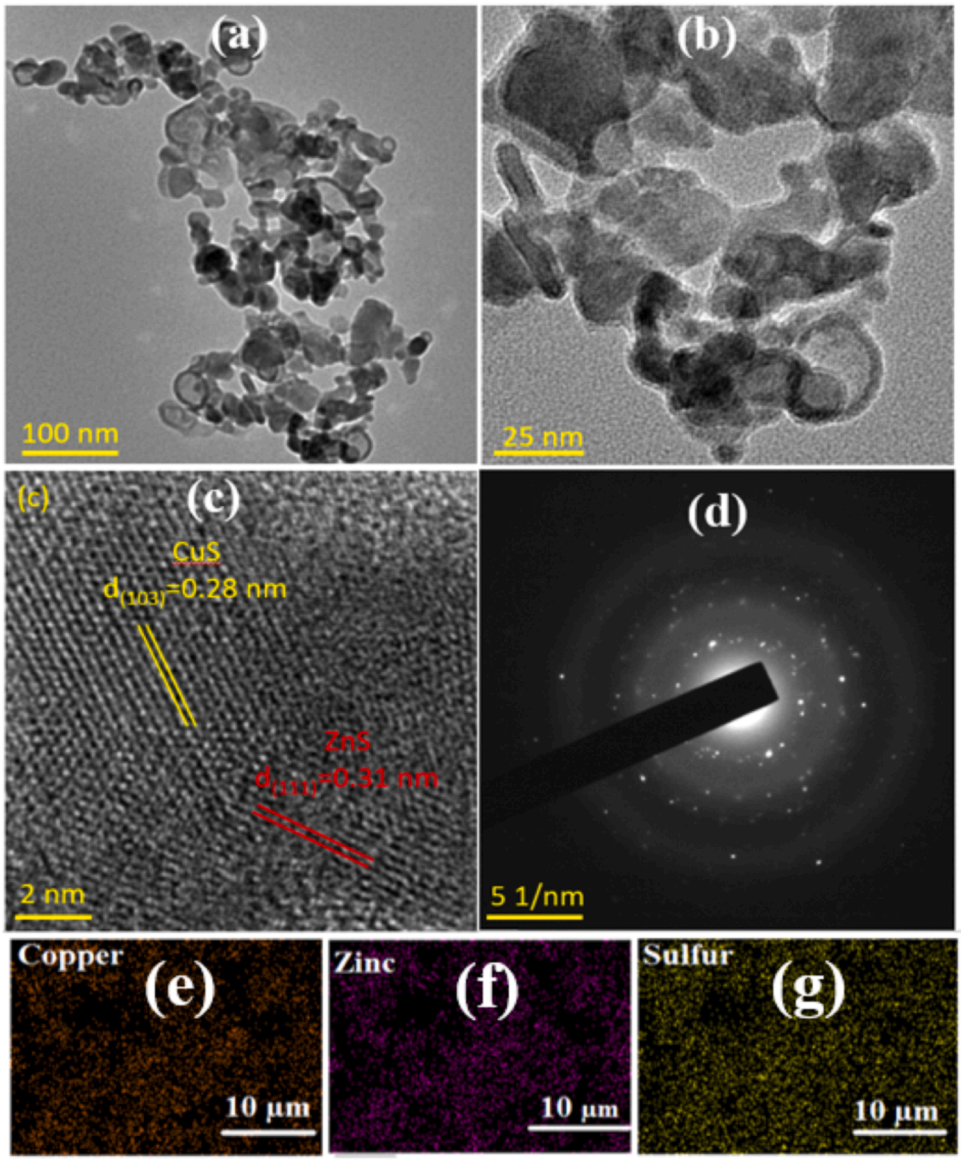

Fig. 5. TEM images of CuS/ZnS composites: **(a-d)** morphology and cristallinity, including lattice spacings of each component, **(e-g)** the elemental mapping showing the distribution of Cu, Zn and S.

enhanced CO production at all potentials, with suppressed H_2 evolution compared to the 1:1 ratio, indicating that higher Cu content favors selective CO_2 reduction over hydrogen evolution. CH_4 and C_2H_4 production are also more pronounced, especially at –1.3 V and –1.5 V, reflecting improved hydrocarbon formation.

Fig. 8c reveals that the 1:2 CuS/ZnS composition strongly favors H_2 evolution at lower overpotentials, where it dominates the product distribution. At more negative potentials, CO and hydrocarbons (CH_4, C_2H_4) appear but less efficiently than in the 2:1 system. Formic acid production is slightly higher than in other samples, particularly at –1.1 V, possibly due to higher ZnS content stabilizing formate intermediates.

A general trend across all catalysts is the increased HER activity at more negative potentials, due to the thermodynamic favorability of proton reduction competing with CO_2 electroreduction. Product selectivity depends on catalyst composition, surface interactions, and intermediate availability(Hori, 2008). The increased HER activity also reflects the electrochemical environment, where distinct anodic and cathodic compartments promote CO_2 reduction, but proton presence and pH gradients at the cathode surface favor H_2 evolution. In $KHCO_3$ electrolyte, bicarbonate buffering mitigates pH changes, but at high negative potentials, water reduction to H_2 becomes unavoidable, especially for catalysts prone to HER (Liu et al., 2016; Wang et al., 2021; Suliman et al., 2024). In our system, composition clearly modulates HER: the Cu-rich S2 (2:1) shows lower H_2 (stronger *CO formation/C–C coupling) and higher CO/C_2H_4 than S1 and the ZnS-rich S3 (1:2), while at more negative potentials HER increasingly suppresses CO_2 products on S3. This agrees with S2's faster kinetics (lower Tafel, lower Rct, Fig. 7), explaining why S2 sustains higher eCO_2RR partial currents under bias (Fig. 8) (Hori, 2008; Liu et al., 2016; Wang et al., 2021)."

Overall, the 2:1 CuS/ZnS catalyst demonstrates the best product distribution for CO_2 reduction, with higher CO and hydrocarbon formation efficiencies and relatively lower H_2 generation indicating improved selectivity and catalytic performance. This underscores the synergistic effect between Cu and Zn species, where optimal Cu enrichment enhances CO_2 activation while modulating hydrogen evolution.

Flow cell electrocatalytic evaluations

In addition to H-cell experiments, the electrocatalytic performance of

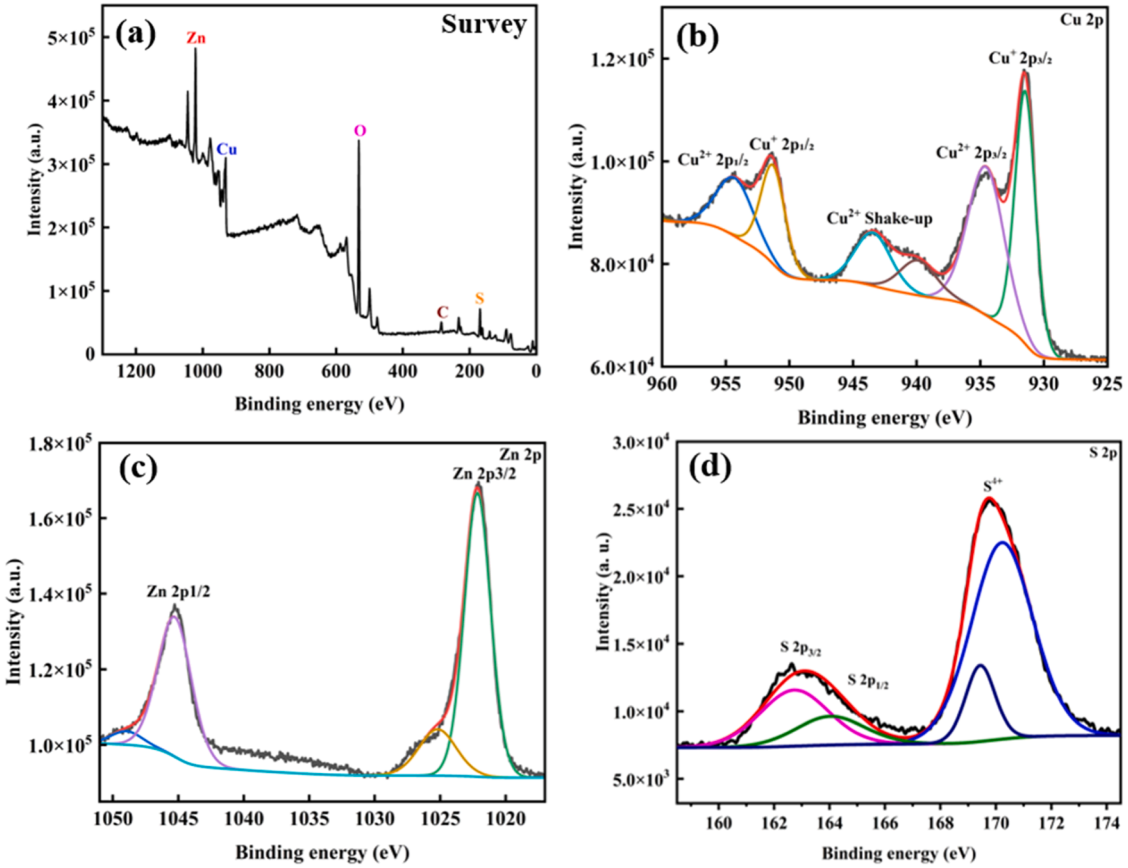

Fig. 6. XPS spectra of CuS/ZnS **(a)** survey spectrum **(b)** Cu 2p, **(c)** Zn 2p and **(d)** S 2p regions.

Table 1
Comparison of the catalytic performance of the S2 catalyst with similar electrocatalysts reported for electroreduction of CO_2.

Catalyst	Applied potential (Vs RHE)	Main product (s)	FE (%)	Ref.
CuS nanosheet arrays	−0.7 V	Formate	70	(Dou et al., 2021)
Cu–S (sulfur-modified Cu)	−0.8 V	Formate	80	(Shinagawa et al., 2018)
CuS/NF (Ni foam-supported)	−1.1 V	CH_4	73	(Mukherjee et al., 2024)
CuS@NF	−1.1 V	CH_4	73.5	(Zhao et al., 2017)
Bi/CeO_2/CuS	−0.9 V	Formate	88	(Wang et al., 2024)
CuS decorated CuO	−0.7 V	Formate	84	(Kahsay et al., 2019)
$Cu_{0.43}Zn_{0.57}O$	−0.95 V	CO	45.4	(Dongare et al., 2021)
TA-ZnS	−1.9 V	CO	80	(Nam et al., 2023)
CuS/ZnS	−1.6	C1 C2	60 % C1, 20 % C2	This Work

CuS, ZnS and CuS/ZnS composite electrodes was evaluated in a flow cell system, this configuration, combined with GDEs, enhances reactant accessibility, improves mass transport, and facilitates efficient charge transfer overcoming CO_2 solubility limitations and enabling higher current densities. Compared with the H-cell, the higher CO_2 flux and improved mass transport in the flow cell comparatively suppress HER, enabling higher CO/C_2H_4 partial currents and selectivity (Figs. 9 and 10) (Wang et al., 2021).

LSV was employed to assess the current response of CuS, ZnS **(SI-**Fig. 3) and CuS/ZnS composite electrodes with different CuS:ZnS ratios (1:1, 2:1, and 1:2 for S1, S2, and S3, respectively) under identical conditions. The LSV results (Fig. 9a) show a clear dependence of current density on electrode composition. Among the three, S2 (CuS: ZnS = 2:1) exhibited the highest current density, reaching ~−280 mA·cm^{-2} at −1.2 V vs. RHE, compared to S1 (−150 mA·cm^{-2}) and S3 (−200 mA·cm^{-2}).

This trend indicates that a higher proportion of CuS improves the electrochemical activity by providing a greater density of electroactive sites, enhanced charge transfer kinetics, and a more conductive electrode interface. Additionally, the presence of ZnS in an optimal ratio can hinder CuS agglomeration, preserving a well-defined surface area with improved reactant accessibility. Furthermore, the use of a flow-cell system in combination with GDEs facilitates higher current densities by improving mass transport and ensuring a steady supply of reactants to the electrode surface (Gao et al., 2023a; Gao et al., 2023b).

A comparison of the materials S1, S2, and S3 highlights the crucial role of composition in controlling charge transport characteristics and overall electrochemical performance. The optimal behavior is observed with S2.

Tafel analysis (Fig. 9b) shows significant differences in the CO_2 reduction kinetics among the CuS/ZnS catalysts. S2 (CuS: ZnS = 2:1) exhibits the lowest Tafel slope (167 mV·dec^{-1}), indicating superior reaction kinetics compared to S1 (254 mV·dec^{-1}) and S3 (358 mV·dec^{-1}).

The stability of the S2 (2:1) CuS/ZnS composite was evaluated over 12 h (Fig. 10a), demonstrating excellent durability and maintaining a high current density of ~170 mA·cm^{-2} with only a minor decline. This indicates strong electrochemical robustness under continuous operation. Faradaic efficiency results (Fig. 10b-d) show the production of ethylene (C_2H_4), formic acid (HCOOH), carbon monoxide (CO), and methane (CH_4) using CuS/ZnS catalysts of different compositions for CO_2 electroreduction.

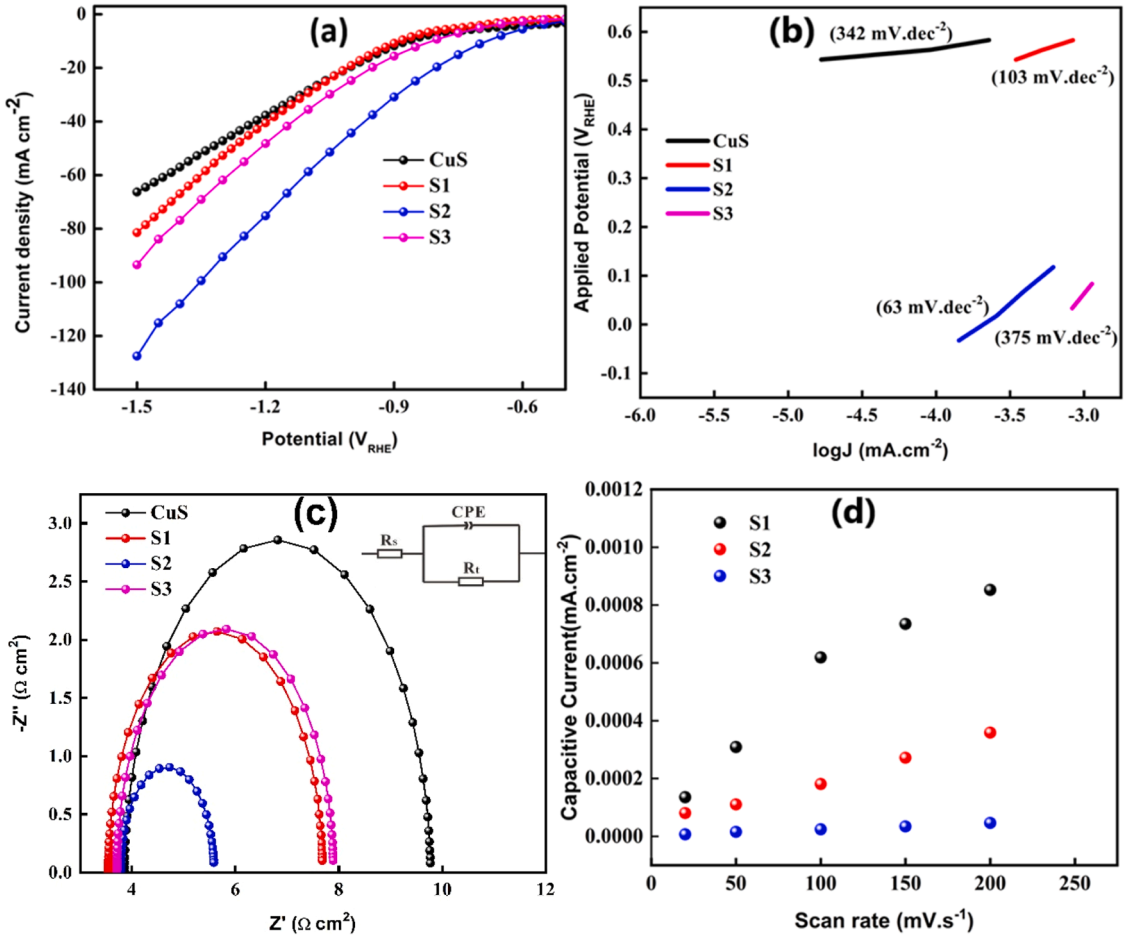

Fig. 7. **(a)** LSV curves, **(b)** Tafel slopes and **(c)** EIS Nyquist plots **(d)** Cdl slops of, CuS/ZnS composites with ratios of 1:1, 2:1 and 1:2 in 0.5 M $KHCO_3$ electrolyte.

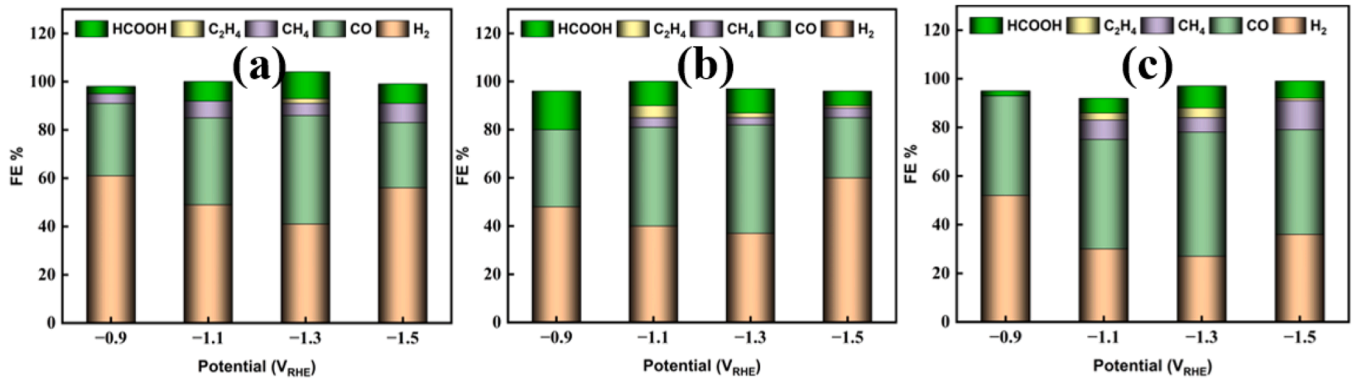

Fig. 8. Faradic efficacies for CO_2 electroreduction in H-cell tests using of CuS/ZnS composites with ratios (a) (1:1), (b) (2:1) and (c) (1:2).

For S1 (1:1 CuS: ZnS), ethylene production remains low across all applied potentials (−1.0 to −1.6 V vs. RHE), indicating limited C–C coupling activity (Fig. 10b). The moderate yield of formic acid suggests that a balanced CuS/ZnS ratio provides active sites favoring partial CO_2 reduction. This aligns with literature reporting that Cu sites can stabilize intermediates necessary for C_2H_4 formation. Additionally, moderate CO and CH_4 generation indicates that the surface moderately supports both single-carbon and multi-carbon pathways.

In contrast, S2 (2:1 CuS/ZnS) shows a significantly higher FE for ethylene (~20 %) at more negative potentials (Fig. 10c) suggesting enhanced C–C coupling. This behavior is attributed to Cu-rich surfaces, which are known to facilitate CO adsorption and hydrogenation, thus promoting ethylene formation. The lower formic acid FE observed in S2 suggests a shift in selectivity toward multi-carbon products due to the increased Cu content, which favors CO dimerization over single-carbon pathways. The presence of both CO and CH_4 further supports the hypothesis that the catalyst surface facilitates CO formation and subsequent hydrogenation to CH_4. The overall performance of the optimized CuS/ZnS (2:1) catalyst can also be evaluated in terms of energy conversion efficiency (ECE), which accounts for both Faradaic efficiency and applied potential. At −1.2 V vs. RHE in the flow-cell configuration, the catalyst achieves ~60 % FE for C_1 products and ~20 % for C_2H_4, corresponding to an estimated ECE of ~20–25 %. These values are in good agreement with state-of-the-art Cu-based systems reported in

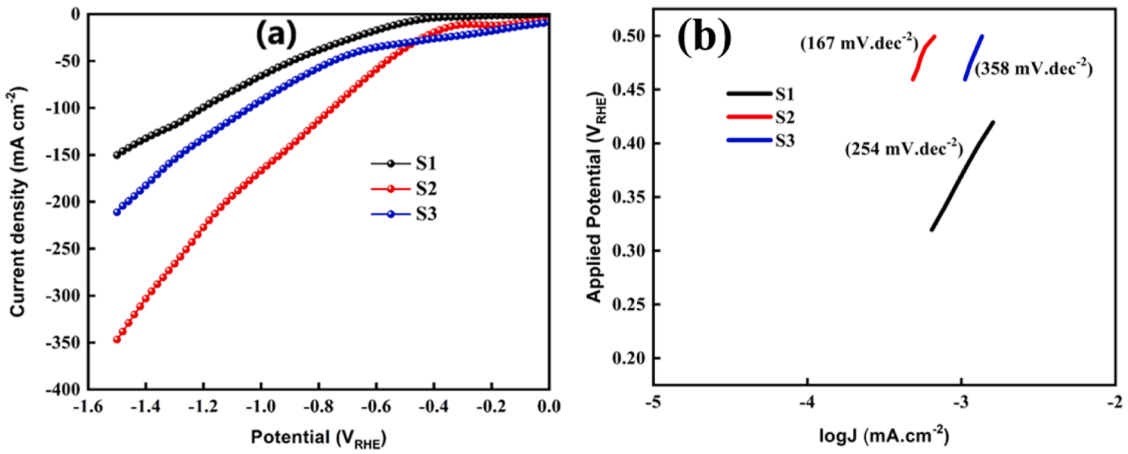

Fig. 9. **(a)** LSV curves **(b)** Tafel slopes of CuS/ZnS composites with different ratios (1:1, 2:1 and 1:2) in 1 M KOH electrolyte.

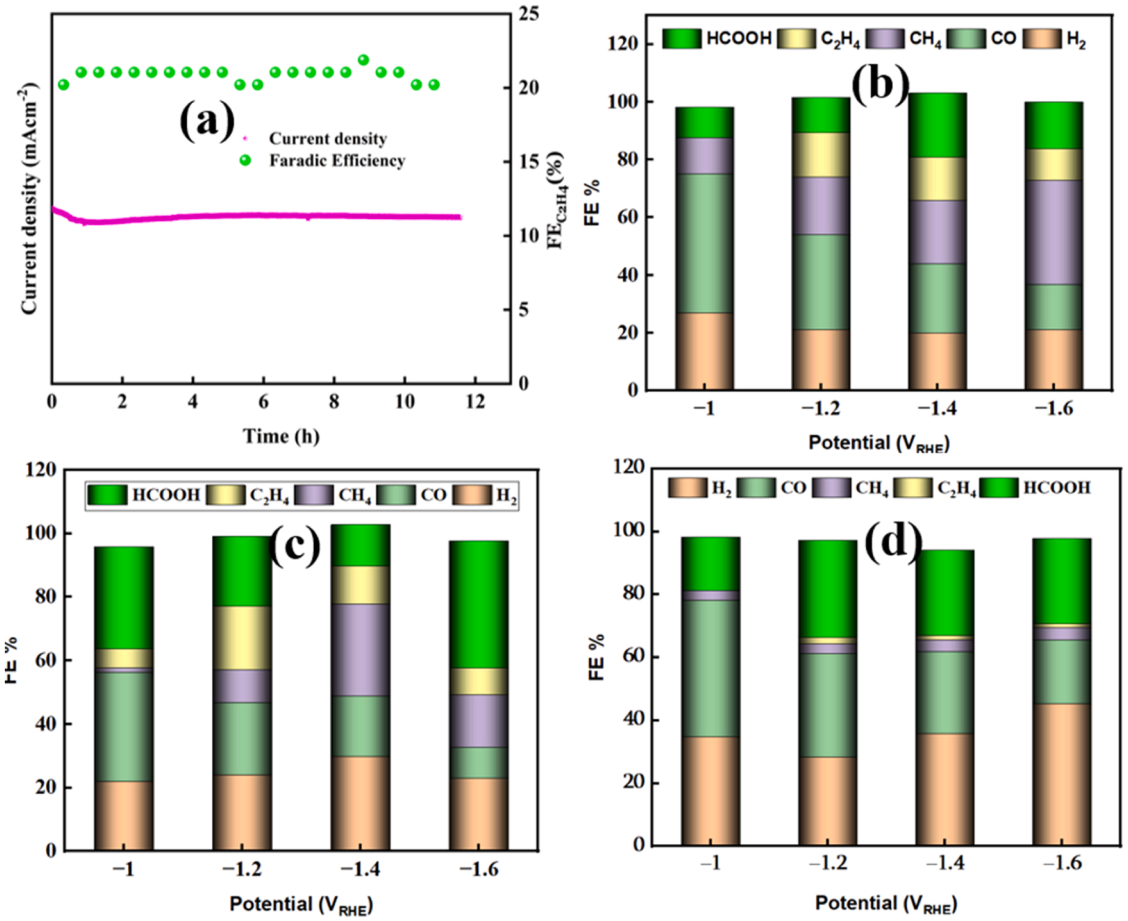

Fig. 10. **(a)** Stability test of CuS/ZnS (2:1); Faradic efficiencies (in Flow-cell tests) of **(b)** CuS/ZnS (1:1), **(c)** CuS/ZnS (2:1) and **(d)** CuS/ZnS (1:2).

literature, confirming the competitiveness of our CuS-based composite approach (Nitopi et al., 2019; Dinh et al., 2018). Importantly, this analysis highlights that the synergy of CuS/ZnS interfacial active sites with the alkaline flow-cell environment not only enhances activity and selectivity but also provides an energetically favorable route for sustainable CO_2 conversion.

S3 (1:2 CuS: ZnS), with a higher ZnS content, displays a low FE for ethylene (Fig. 10d) suggesting that ZnS promotes single-carbon product pathways. The high FE for formic acid implies that Zn sites efficiently stabilize *OCHO intermediates, favoring HCOOH production. Substantial CO generation indicates that ZnS-rich surfaces catalyze the reduction of CO_2 to CO effectively. Meanwhile, the low production of ethylene and methane further confirms that increasing ZnS content suppresses C–C coupling and multi-electron transfer, shifting selectivity toward single-carbon products.

Overall, this comparative investigation demonstrates that the CuS: ZnS ratio plays a key role in controlling the selectivity toward formic acid, ethylene, CO, and methane. CuS-rich compositions promote C_2H_4 and CH_4 formation via enhanced CO hydrogenation and C–C coupling, while ZnS-rich systems favor CO and HCOOH generation through

stabilization of single-carbon intermediates such as *OCHO(Suliman et al., 2024; Suliman et al., 2023). Faradic efficacies for CuS and ZnS at different potentials are shown in **SI**-Fig. 4.

The CuS/ZnS catalyst is highly effective for formic acid production in CO_2 reduction. While some reported catalysts (Table 1) such as CuS and Cu_2SnS_3/CuS show comparable performance at specific potentials, the CuS/ZnS system presented here demonstrates competitive activity and selectivity, highlighting the importance of optimizing both catalyst composition and operating potential for efficient CO_2 conversion (Fig. 11).

Recent eCO_2RR research covers catalyst materials and structures, catalyst chemistry, product selectivity, and reaction mechanisms; work on molecular catalysts is also widespread. For completeness, we include a brief mechanism primer: CO_2 is activated to *COOH and *CO; C_1 products arise via *CO hydrogenation ($CO/HCOO^-/CH_4$), while C_2^+ products form through *CO–*CO coupling to *$OCCO^-$ accompanied by balanced half-reactions to anchor these pathways.

*CO-pathway (Cu): CO_2 → *COOH → *CO; C_1 products form by hydrogenation of *CO, while C–C coupling of adjacent *CO → *OCCO leads to C_2 products (e.g., C_2H_4), consistent with canonical Cu mechanisms (Hori, 2008; Wang et al., 2021).

(R1) CO: $CO_2 + H_2O + 2e^- \rightarrow CO + 2OH^-$

(R2) Formate: $CO_2 + H_2O + 2e^- \rightarrow HCOO^- + OH^-$

(R3) Methane: $CO_2 + 6H_2O + 8e^- \rightarrow CH_4 + 8OH^-$

(R4) Ethylene: $2CO_2 + 8H_2O + 12e^- \rightarrow C_2H_4 + 12OH^-$

Computational modeling of eCO_2RR at CuS/ZnS (1:1) structure and adsorption energies

To gain deeper insight into the preferential formation of the CO_2 conversion products on the CuS/ZnS catalyst, we performed computational analyses to evaluate the adsorption energies of key reaction intermediates. Fig. 12 presents the optimized and unoptimized structures involved in the conversion pathway from CO_2 to HCOOH. In this context, an asterisk (*) preceding an adsorbate (e.g., *CO_2) denotes adsorption of that species onto the catalyst surface. The atoms in the structural models are color-coded as follows: brown for carbon, black for zinc, blue for copper, yellow for sulfur, red for oxygen, and white for hydrogen. Upon interaction of CO_2 with the catalyst surface, a significant electronic and structural transformation occurs, as evidenced by the elongation of the C=O bond from 1.19 Å to 2.74 Å. This change reflects the activation of CO_2, where its antibonding π* orbitals accept electron density from copper atoms, leading to the cleavage of the C=O double bond and the formation of a strong Cu–O coordination bond. This interaction results in a CO_2^- intermediate, which facilitates further reduction to other products. Additionally, the Cu–Zn bonding is strengthened, as indicated by a decrease in bond length (see Figs. 12a-b) highlighting charge redistribution across the Cu–Zn–S network as copper atoms gain or lose electron density during CO_2 coordination.

The moderate adsorption energy, E_{ads}, observed for CO_2 indicates that while the molecule is activated upon adsorption, a portion remains unreactive compared to other intermediates. Among all adsorbates, *COOH exhibits the lowest adsorption energy (E_{ads} = 0.99 eV), which is also lower than that of *HCOO (E_{ads} = 1.49 eV). This suggests that the pathway from CO_2 to *CO via *HCOO is energetically favorable, promoting strong *CO adsorption and facilitating C–C coupling, a key step for the formation of C_2 products such as C_2H_4, as supported by our experimental results (Fig. 10b). Additionally, the CO_2-to-HCOOH pathway is also favorable, as evidenced by the strong binding of *HCOO. The chemisorption of C–S in *COOH, illustrated in Fig. 12f, demonstrates the expected cleavage of the O–C–O bond, leading to the formation of O–H and O species, which in turn favors oxygen evolution reactions rather than the formation of other products (see Figs. 12e-f) Notably, the relatively high E_{ads} values for *CO and *HCOOH indicate that while these species are strongly adsorbed, the interaction transitions from chemisorption to physisorption, enhancing their desorption. As a result, both CO and HCOOH exhibit moderate to high selectivity as products.

Thermochemistry, free-energy profiles, and adsorption energies

Thermochemical data for adsorbates and complexes are presented in Table 2. For complex systems, labels such as *CO_2-O-Ter-Cu, indicate that the oxygen atom of the CO_2 molecule is positioned atop a copper site on the CuS/ZnS catalyst. However, this notation does not imply that the intermediate interacts exclusively with copper; rather, it denotes the primary termination site used in the computational model.

Based on thermochemistry, the free energies were calculated, and free-energy diagrams were drawn to understand and compare the favorable pathways and possible formation of $CO_{(gas)}$ and $HCOOH_{(liquid)}$ on the catalyst, as shown in Fig. 13. Fig. 13a shows the free energy profile for adsorbates terminated on Cu. In contrast, Fig. 13b shows the free energy profile for adsorbates terminated on S. Both terminations showed no considerable differences in their profiles except for *COOH formation, which was better in Cu termination than S. From free energy diagrams, the $*CO_2 \rightarrow *HCOO \rightarrow *CO \rightarrow CO_{(gas)}$ was found to be the most favorable and spontaneous pathway to produce $CO_{(gas)}$, while the pathway $*CO_2 \rightarrow *HCOO \rightarrow *HCOOH \rightarrow HCOOH_{(liquid)}$ is less spontaneous than CO.

Our experimental results revealed that, in most cases, $CO_{(gas)}$ was produced in greater quantities than $HCOOH_{(liquid)}$. However, at higher applied potentials, such as –1.6 V (vs. RHE), the production levels of CO and HCOOH became approximately equal. The observed increase in HCOOH formation at elevated potential can be attributed to the higher adsorption energies identified through DFT calculations (see Figs. 12i-j). Further detailed mechanistic investigation, particularly exploring the pathways leading to C_2H_4 and CH_4 formation with varying CuS and ZnS ratios, would provide valuable insights and could be pursued as an extension of this work.

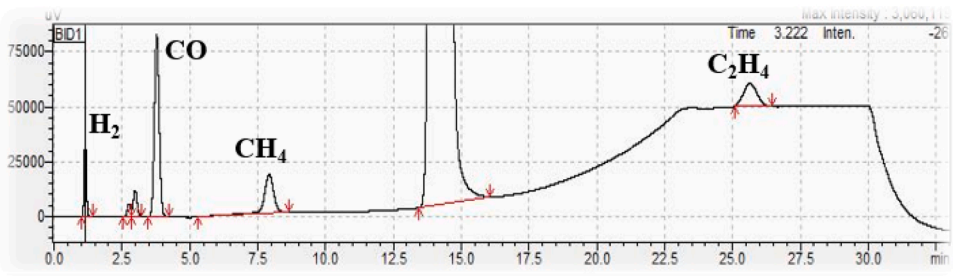

Fig. 11. GC-BID chromatogram of the detected products.

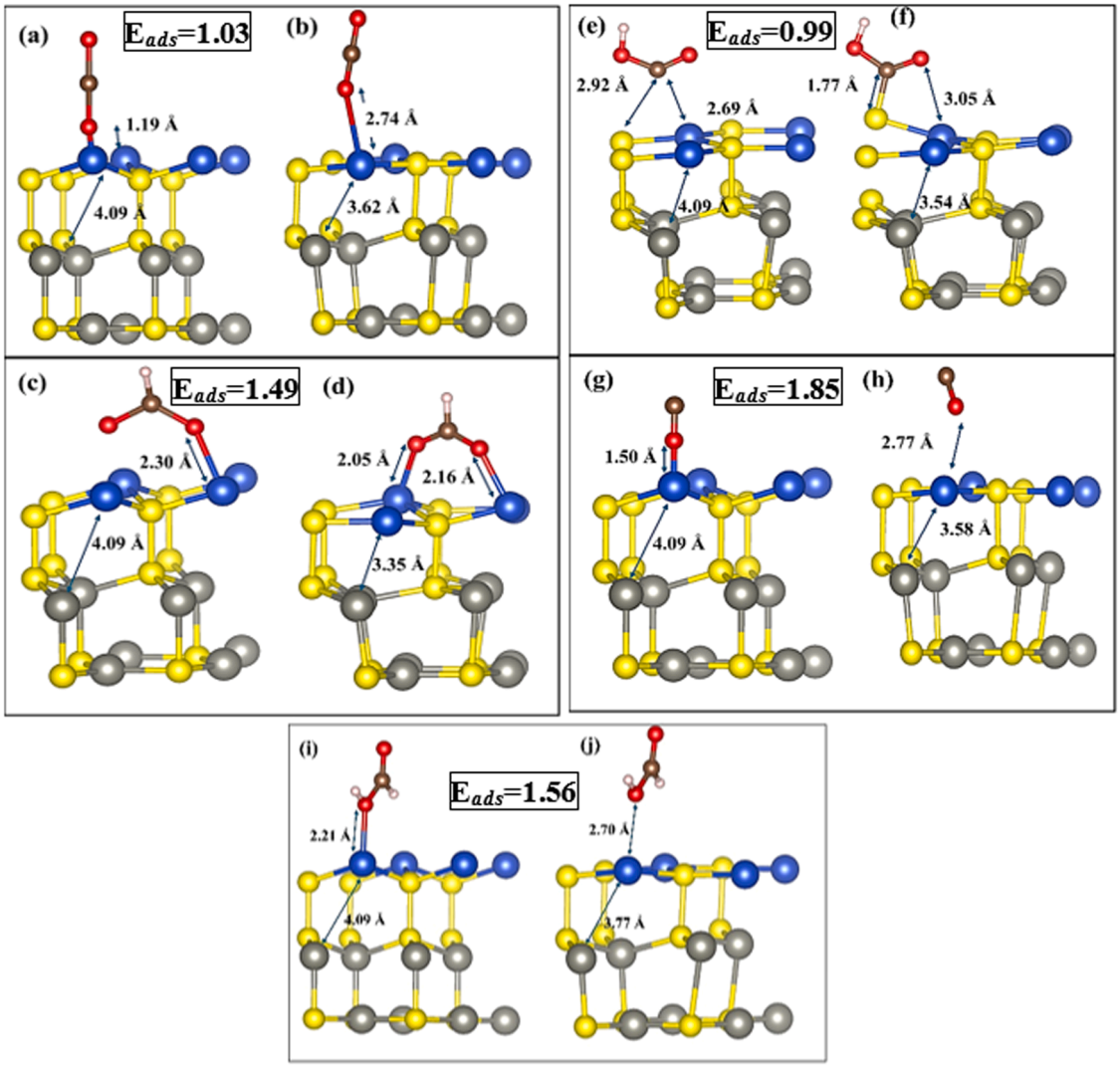

Fig. 12. Change in geometry before and after optimization of CuS/ZnS (1:1) with adsorption energies (E_{ads}) in eV for **(a)** CO_2 before optimization, **(b)** CO_2 after optimization, **(c)** HCOO before optimization, **(c)** HCOO after optimization, **(e)** COOH before optimization, **(f)** COOH after optimization, **(g)** CO before optimization, **(h)** CO after optimization, **(i)** HCOOH before optimization, **(j)** HCOO after optimization.

Table 2
Thermochemical properties extracted from optimized structures using vibrational analysis in CP2K.

Name	Entropy (S) *kJ/mol·K*	Heat capacity *kJ/mol·K*	Enthalpy correction (H-U) *kJ/mol*	Free Energy (E) *eV*
*CO_2	0.00	0.00	0.00	0
*	0.02	0.05	584.59	−0.602
H_2	0.14	0.03	34.48	−0.06
CO_2	0.22	0.04	39.37	−0.27
CO	0.20	0.03	21.25	−0.39
COOH	0.22	0.04	61.93	−0.04
HCOO	0.22	0.04	53.65	−0.13
HCOOH	0.23	0.04	95.20	0.30
*CO_2-O-Ter-Cu	0.05	0.09	689.30	0.702
*CO_2-O-Ter-S	0.04	0.09	679.28	0.693
*CO-O-Ter-Cu	0.04	0.09	584.31	0.596
*CO-O-Ter-S	0.05	0.09	585.78	0.596
*HCOO-O-Ter-Cu	0.05	0.10	624.52	0.635
*HCOOH-O-Ter-Cu	0.04	0.07	1165.33	1.198

Conclusion

In this work, we demonstrated the enhanced performance of CuS/ZnS nanocomposites for electrochemical CO_2 reduction, particularly in achieving valuable multi-product selectivity yielding up to 60 % C_1 products and 20 % ethylene (C_2H_4). The most efficient catalyst was identified as the 2:1 CuS/ZnS composition (S2), which exhibited a high Faradaic efficiency (~20 %) for ethylene production at a current density of 280 mA·cm^{-2} in a flow-cell configuration. This represents a significant improvement in CO_2 conversion efficiency, highlighting its potential for scalable and sustainable applications.

The mechanistic role of the CuS/ZnS ratio in determining product selectivity was elucidated, withDFT calculations providing molecular-level validation of the experimental results, confirming the reliability and reproducibility of the observed catalytic behavior. Cu-rich sites in S2 were found to promote C–C coupling, favoring the formation of ethylene and formic acid. In H-cell experiments, the increased production of CO and hydrocarbons, along with the suppression of H_2 evolution, demonstrated enhanced selectivity and catalytic efficiency. This underscores the synergistic interaction between Cu and Zn species, where optimal Cu enrichment facilitates CO_2 activation while minimizing competitive hydrogen evolution.

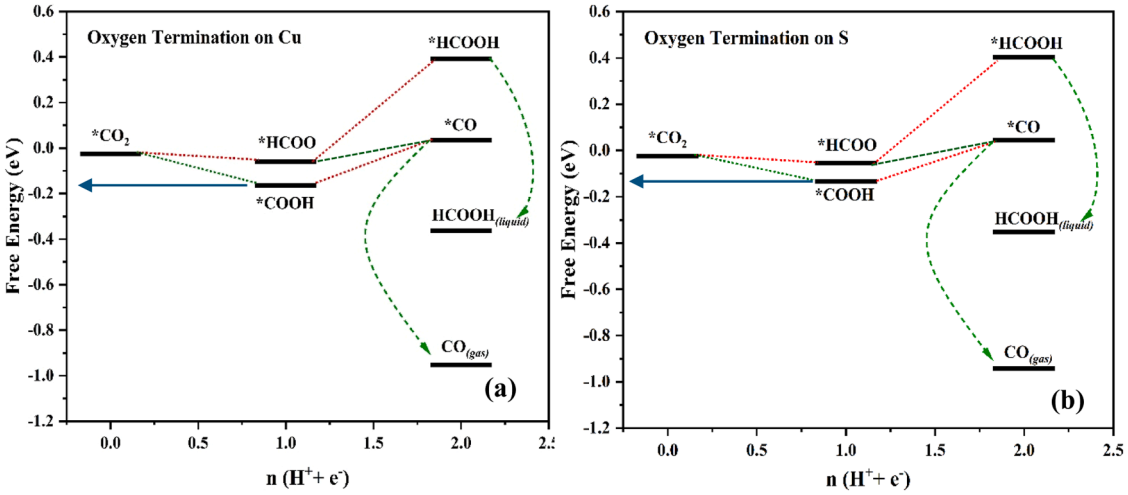

Fig. 13. Free-energy diagrams of CuS/ZnS (1:1) for **(a)** oxygen terminated on copper and **(b)** oxygen terminated on sulfur.

The use of GDEs in the flow-cell configuration enabled higher current densities and improved reactant availability, significantly boosting ethylene production, which was negligible in the H-cell setup. These findings emphasize the critical roles of electrolyte composition, catalyst architecture, and reactor design in controlling both the nature and distribution of CO_2 reduction products. Density functional theory calculations revealed that the *COOH pathway on the CuS/ZnS catalyst strongly favors the formation of CO and HCOOH, providing molecular-level validation for the observed product selectivity.

By tuning the CuS/ZnS ratio, this work lays the foundation for the rational design of next-generation electrocatalysts capable of high-efficiency and scalable CO_2 conversion. Ultimately, the results pave the way for future advancements in electrocatalysis, where engineered flow-cell systems could drive selective C_2 product formation and contribute to global efforts in CO_2 mitigation and the circular carbon economy.

CRediT authorship contribution statement

Naimat Ullah: Writing – original draft, Investigation. **Munzir H. Suliman:** Writing – review & editing, Resources, Conceptualization. **Sikandar Khan:** Writing – review & editing, Funding acquisition. **Zubair Ahmed Laghari:** Software, Validation, Writing – review & editing. **Guillermo Diaz-Sainz:** Writing – review & editing. **Abdulmajeed Hendi:** Software, Validation, Writing – review & editing. **Wan Zaireen Nisa Yahya:** Software, Validation, Writing – review & editing. **Muhammad Usman:** Writing – review & editing, Supervision, Investigation, Conceptualization.

Declaration of competing interest

The authors guarantee that there are no conflicts of interest, both financial and personal, that could have impacted the research or findings presented within this paper.

Acknowledgements

The author would like to acknowledge the support provided by King Fahd University of Petroleum & Minerals (KFUPM) and the support from the Saudi Aramco Chair Professor Program at KFUPM No ORCP2390

Supplementary materials

Supplementary material associated with this article can be found, in the online version, at doi:10.1016/j.ccst.2025.100532.

References

Abdinejad, M., Seifitokaldani, A., Dao, C., Sargent, E.H., Zhang, X.-A., Kraatz, H.B., 2019. Enhanced electrochemical reduction of CO_2 catalyzed by cobalt and iron amino porphyrin complexes. ACS Appl. Energy Mater. (Basel) 2, 1330–1335.

Abdinejad, M., Subramanian, S., Motlagh, M.K., Noroozifar, M., Duangdangchote, S., Neporozhnii, I., Ripepi, D., Pinto, D., Li, M., Tang, K., 2023. Insertion of MXene-based materials into Cu–Pd 3D aerogels for electroreduction of CO_2 to formate. Adv. Energy Mater. 13, 2300402.

Chen, Z., Ma, Z., Fan, G., Li, F., 2024. Critical role of Cu nanoparticle-loaded Cu (100) surface structures on structured copper-based catalysts in boosting ethanol generation in CO2 electroreduction. ACS Appl. Mater. Interfaces 16, 35143–35154.

Ding, M., Chen, Z., Liu, C., Wang, Y., Li, C., Li, X., Zheng, T., Jiang, Q., Xia, C., 2023. Electrochemical CO_2 reduction: progress and opportunity with alloying copper. Mater. (Basel) Rep.: Energy 3, 100175.

Dinh, C.-T., Burdyny, T., Kibria, M.G., SeifitokaldanI, A., Gabardo, C.M., García DE Arquer, F.P., Kiani, A., Edwards, J.P., DE Luna, P., Bushuyev, O.S., 2018. CO_2 electroreduction to ethylene via hydroxide-mediated copper catalysis at an abrupt interface. Science 360, 783–787.

Doğan, B., Shahbaz, M., Bashir, M.F., Abbas, S., Ghosh, S., 2023. Formulating energy security strategies for a sustainable environment: evidence from the newly industrialized economies. Renew. Sustain. Energy Rev. 184, 113551.

Dongare, S., Singh, N., Bhunia, H., Bajpai, P.K., 2021. Electrochemical reduction of CO_2 using oxide based Cu and Zn bimetallic catalyst. Electrochim. Acta 392, 138988.

Dou, T., Qin, Y., Zhang, F., Lei, X., 2021. CuS nanosheet arrays for electrochemical CO_2 reduction with surface reconstruction and the effect on selective formation of formate. ACS Appl. Energy Mater. (Basel) 4, 4376–4384.

Fields, M., Hong, X., Nørskov, J.K., Chan, K., 2018. Role of subsurface oxygen on Cu surfaces for CO_2 electrochemical reduction. J. Phys. Chem. (Easton) C 122, 16209–16215.

Gao, Q., Zhou, L., Xu, S., Dai, S., Zhu, Q., Li, Y., 2023a. Significant improvement and mechanism of tetracycline degradation with the synergistic piezoelectric effect of ZnO/CuS Z-scheme heterojunction photocatalysts. Environ. Sci.: Nano 10, 581–594.

Gao, Y., Guo, Y., Zou, Y., Liu, W., Luo, Y., Liu, B., Zhao, C., 2023b. Hydrothermal synthesis of CuS catalysts for electrochemical CO_2 reduction: unraveling the effect of the sulfur precursor. ACS Appl. Energy Mater. (Basel) 6, 1340–1354.

Guo, Y., luo, Y., Wang, H., Chen, X., Liu, X., Guo, B., Sun, J., Wang, R., Li, W., Zhao, C., 2025. Mediating Zn loading on Cu-Zn bimetallic catalyst for electrochemical CO_2 reduction into tunable syngas. Fuel 392, 134821.

Hori, Y., 2008. Electrochemical CO2 reduction on metal electrodes. Mod. Asp. Electrochem. 89–189.

Hori, Y., Takahashi, I., Koga, O., Hoshi, N., 2003. Electrochemical reduction of carbon dioxide at various series of copper single crystal electrodes. J. Mol. Catal. A: Chem. 199, 39–47.

Huang, Y., Kuldasheva, Z., Bobojanov, S., Djalilov, B., Salahodjaev, R., Abbas, S., 2023. Exploring the links between fossil fuel energy consumption, industrial value-added, and carbon emissions in G20 countries. Environ. Sci. Pollut. Res. 30, 10854–10866.

Jan, F.A., Ullah, R., Ullah, N., Salam, A., 2022. An investigation into the environmental and therapeutic applications of holmium-doped titanium dioxide (Ho-TiO_2) nanocatalysts: a kinetic and thermodynamic study of the photocatalytic degradation of Safranin O dye. Nano Futures 6, 015003.

Jia, S., Zhu, Q., Han, S., Zhai, J., Dong, M., Xia, W., Xing, X., Wu, H., He, M., Han, B., 2023. Ultra-fast synthesis of three-dimensional porous Cu/Zn heterostructures for enhanced carbon dioxide electroreduction. Chem. Sci. 14, 11474–11480.

Juntrapirom, S., Santatiwongchai, J., Watwiangkham, A., Suthirakun, S., Butburee, T., Faungnawakij, K., Chakthranont, P., Hirunsit, P., Rungtaweevoranit, B., 2021. Tuning CuZn interfaces in metal–organic framework-derived electrocatalysts for enhancement of CO_2 conversion to C 2 products. Catal. Sci. Technol. 11, 8065–8078.

Kahsay, A.W., Ibrahim, K.B., Tsai, m.-C., Birhanu, M.K., Chala, S.A., Su, W.-N., Hwang, B.-J, 2019. Selective and low overpotential electrochemical CO 2 reduction to formate on CuS decorated CuO heterostructure. Catal. Lett. 149, 860–869.
Karikalan, N., Karthik, R., Chen, S.-M., Karuppiah, C., Elangovan, A., 2017. Sonochemical synthesis of sulfur doped reduced graphene oxide supported CuS nanoparticles for the non-enzymatic glucose sensor applications. Sci. Rep. 7, 2494.
Kas, R., Hummadi, K.K., Kortlever, R., De Wit, P., Milbrat, A., Luiten-Olieman, M.W., Benes, N.E., Koper, M.T., Mul, G., 2016. Three-dimensional porous hollow fibre copper electrodes for efficient and high-rate electrochemical carbon dioxide reduction. Nat. Commun. 7, 10748.
Khan, S., Mahmood, A., Shah, A.U.H.A., Rahman, G., Khan, A., Ullah, N., 2022. Challenges and innovative strategies related to synthesis and electrocatalytic/energy storage applications of metal sulfides and its derivatives. J. Electroanal. Chem. (Easton) 923, 116760.
Kong, C., Jiang, G., Sheng, Y., Liu, Y., Gao, F., Liu, F., Duan, X., 2023. Progress on Cu-based metal-organic frameworks for high-efficiency electrochemical CO_2 conversion. Chem. Eng. J. 460, 141803.
Kühne, T.D., Iannuzzi, M., Del Ben, M., Rybkin, V.V., Seewald, P., Stein, F., Laino, T., Khaliullin, R.Z., Schütt, O., Schiffmann, F., 2020. CP2K: an electronic structure and molecular dynamics software package-Quickstep: efficient and accurate electronic structure calculations. J. Chem. Phys. 152.
Laghari, Z.A., Yahya, W.Z.N., Mohammed, S.A.S., Bustam, M.A., 2025. Electrocatalytic pathways and efficiency of cuprous oxide (Cu2O) surfaces in CO_2 electrochemical reduction (CO2ER) to methanol: a computational approach. Catalysts 15, 130.
Lazanas, A.C., Prodromidis, M.I., 2023. Electrochemical impedance spectroscopy– a tutorial. ACS Meas. Sci. Au 3, 162–193.
Li, M., Hu, Y., Wu, T., Sumboja, A., Geng, D., 2023. How to enhance the C2 products selectivity of copper-based catalysts towards electrochemical CO2 reduction?—A review. Mater. (Basel) Today 67, 320–343.
Liu, M., Pang, Y., Zhang, B., De luna, P., Voznyy, O., Xu, J., Zheng, X., Dinh, C.T., Fan, F., Cao, C., 2016. Enhanced electrocatalytic CO_2 reduction via field-induced reagent concentration. Nature 537, 382–386.
Luo, Y., Chen, X., Liu, X., Guo, Y., Gao, Y., Zhao, G., Zhao, C., 2024. Electrochemical CO_2 reduction to syngas on copper mesh electrode: alloying strategy for tuning syngas composition. Carbon N Y Capture Sci. Technol. (Singap World Sci.) 13, 100254.
Mcglynn, J.C., Dankwort, T., Kienle, L., Bandeira, N.A., Fraser, J.P., Gibson, E.K., Cascallana-Matías, I., KAMARás, K., Symes, M.D., Miras, H.N., 2019. The rapid electrochemical activation of MoTe2 for the hydrogen evolution reaction. Nat. Commun. 10, 4916.
Mosali, V.S.S., puxty, G., Horne, M.D., Bond, A.M., Zhang, J., 2024. Selective electrochemical methanation of carbon dioxide using a sulphide derived CuZn catalyst. Electrochim. Acta 475, 143628.
MukherjeE, A., Abdinejad, M., Mahapatra, S.S., Ruidas, B.C., 2024. Controlled synthesis of copper sulfide-associated catalysts for electrochemical reduction of CO_2 to Formic acid and beyond: a review. Energy Adv.
Nam, H.-I., Park, K.R., Choi, Y.-W., Sim, H.-J., Sohn, K.Y., Lim, D.-H., 2023. Electrocatalytic CO2 reduction using self-supported zinc sulfide arrays for selective CO production. Appl. Surf. Sci. 612, 155646.
Nitopi, S., Bertheussen, E., Scott, S.B., Liu, X., Engstfeld, A.K., Horch, S., Seger, B., Stephens, I.E., Chan, K., Hahn, C., 2019. Progress and perspectives of electrochemical CO_2 reduction on copper in aqueous electrolyte. Chem. Rev. 119, 7610–7672.
Patel, N., Mehta, D., 2023. The asymmetry effect of industrialization, financial development and globalization on CO_2 emissions in India. Int. J. Thermofluids 20, 100397.
Ramalho, J.P.P., Gomes, J.R., Illas, F., 2013. Accounting for van der Waals interactions between adsorbates and surfaces in density functional theory based calculations: selected examples. RSC Adv. 3, 13085–13100.
Schütt, O., Vandevondele, J., 2018. Machine learning adaptive basis sets for efficient large scale density functional theory simulation. J. Chem. Theory Comput. 14, 4168–4175.
Shinagawa, T., LarrazábaL, G.O., Martín, A.J., Krumeich, F., Pérez-RAMÍREZ, J., 2018. Sulfur-modified copper catalysts for the electrochemical reduction of carbon dioxide to formate. ACS Catal. 8, 837–844.
Skúlason, E., Tripkovic, V., Björketun, M.E., Gudmundsdóttir, S., Karlberg, G., Rossmeisl, J., Bligaard, T., Jónsson, H., Nørskov, J.K., 2010. Modeling the electrochemical hydrogen oxidation and evolution reactions on the basis of density functional theory calculations. J. Phys. Chem. (Easton) C 114, 18182–18197.
Song, Y., Wang, Y., Shao, J., Ye, K., Wang, Q., Wang, G., 2021. Boosting CO_2 electroreduction via construction of a stable ZnS/ZnO interface. ACS Appl. Mater. Interfaces 14, 20368–20374.
Stefan, M., Toloman, D., Popa, A., Mesaros, A., Vasile, O., Leostean, C., Pana, O., 2016. Interface charge transfer process in ZnO: Mn/ZnS nanocomposites. J. Nanoparticle Res. 18, 59.
Suliman, M., Usman, M., ABdelnaby, M., 2023. Synthesis of Bi-metallic zinc–Copper oxide derived from copper MOF for the electrochemical CO_2 reduction to value added products. In: 244th ECS Meeting. ECS. October 8-122023.
Suliman, M.H., AL Naji, H., Usman, M., 2024. Zn-Cu bimetallic gas diffusion electrodes for electrochemical reduction of CO2 to ethylene. Electrochim. Acta 500, 144723.
Suliman, M.H., Usman, M., AL Naji, H., AbdinejaD, M., Ullah, N., HelaL, A., Abdelnaby, M.M., Díaz-Sainz, G., Centi, G., 2025. CO_2 electroreduction to C2 products on bimetallic silver copper melamine complexes. Carbon N Y Capture Sci. Technol. (Singap World Sci.) 14, 100355.
Suliman, M.H., Yamani, Z.H., Usman, M., 2022. Electrochemical reduction of CO_2 to C1 and C2 liquid products on copper-decorated nitrogen-doped carbon nanosheets. Nanomaterials 13, 47.
Tang, Z., Pan, Y., Zhao, Q., Cao, Y., Su, C., Gao, P., Liu, Z., Chen, Y., Li, G., Wang, Q., 2024. Room-temperature synthesis of nonstoichiometric copper sulfide (Cu 2− x S) for sodium ion storage. Inorg. Chem. Front. 11, 3811–3819.
Ullah, N., Shah, S.S., Suliman, M.H., Ismail, F., Kaci, S., Saidina Amin, Usman, M., 2025. Electrochemical CO2 Reduction: A Review toward Sustainable Energy Conversion and Storage. Energy & Fuels 41, 19614–19646.
USman, M., Ghanem, A.S., Niaz Ali Shah, S., Garba, M.D., Yusuf Khan, M., Khan, S., Humayun, M., Laeeq Khan, A., 2022. A review on SAPO-34 zeolite materials for CO_2 capture and conversion. Chem. Rec. (Wash.) 22, e202200039.
Usman, M., Suliman, M.H., 2023. Silver-doped zeolitic imidazolate framework (Ag@ ZIF-8): an efficient electrocatalyst for CO2 conversion to syngas. Catalysts 13, 867.
Usman, M., Suliman, M.H., Abdinejad, M., Kok, J., AL Naji, H., Helal, A., Yamani, Z.H., Centi, G., 2025a. Highly efficient CO_2 electroreduction to formate using Bismuth nanodots within ZIF-8 scaffold. Carbon N Y Capture Sci. Technol. (Singap World Sci.), 100450.
Usman, M., Suliman, M.H., Salihu, I.M., Ullah, N., Abdelnaby, M.M., Abdelsamie, M., 2025b. Cadmium Functionalized Zeolitic Imidazolate framework (Cd-ZIF-8) electrocatalysts for efficient CO_2 conversion to Syngas. ACS Omega (Westport) 10, 20142–20149.
Vs, G.k., Mahesha, M., 2021. XPS analysis of ZnS0. 4Se0. 6 thin films deposited by spray pyrolysis technique. J. Electron Spectros Relat. Phenom. 249, 147072.
Wang, G., Chen, J., Ding, Y., Cai, P., Yi, L., Li, Y., TU, C., Hou, Y., Wen, Z., Dai, L., 2021. Electrocatalysis for CO_2 conversion: from fundamentals to value-added products. Chem. Soc. Rev. 50, 4993–5061.
Wang, L., Chen, H., Xiao, L., Huang, J., 2016. CuS/ZnS hexagonal plates with enhanced hydrogen evolution activity under visible light irradiation. Powder Technol. 288, 103–108.
Wang, L., Nitopi, S., Wong, A.B., Snider, J.L., Nielander, A.C., Morales-Guio, C.G., Orazov, M., Higgins, D.C., Hahn, C., Jaramillo, T.F., 2019. Electrochemically converting carbon monoxide to liquid fuels by directing selectivity with electrode surface area. Nat. Catal. 2, 702–708.
Wang, Q., Bao, T., Zhao, X., Cao, Y., Cao, J., Li, Q., Si, W., 2024. Bi/CeO_2–Decorated CuS electrocatalysts for CO2-to-formate conversion. Molecules 29, 2948.
Wang, Y., Wang, Z., Dinh, C.-T., Li, J., OZden, A., Golam Kibria, M., Seifitokaldani, A., Tan, C.-S., Gabardo, C.M., Luo, M., 2020. Catalyst synthesis under CO_2 electroreduction favours faceting and promotes renewable fuels electrosynthesis. Nat. Catal. 3, 98–106.
Wei, S., Liu, W., Yang, C., Bai, P., Kong, X., Sun, W., Xu, L., 2023. Electronic and geometric modulations of catalysts for electrochemical CO $_2$ reduction reaction. Mater. (Basel) Chem. (Easton) Front. (Boulder) 7, 4723–4743.
Yan, J., Ma, H., Ni, J., Ma, J., Xu, J., Qi, J., Zhu, S., Lu, L., 2023. Engineering iron carbide catalyst with aerophilic and electron-rich surface for improved electrochemical CO_2 reduction. J. Colloid Interface Sci. 648, 558–566.
Yan, J., Song, W., Zhao, Z., Zhang, M., Wu, Y., Zhang, L., 2024. Research progress of copper-based catalysts for CO_2 electrochemical reduction. Int. J. Hydrog. Energy 89, 664–685.
Yang, K., Sun, Y., Chen, S., Li, M., Zheng, M., Ma, L., Fan, W., Zheng, Y., Li, Q., Duan, J., 2023. Less-coordinated atomic copper-dimer boosted carbon–Carbon coupling during electrochemical CO_2 reduction. Small 19, 2301536.
Zhang, J., Guo, C., Fang, S., Zhao, X., Li, L., Jiang, H., Liu, Z., Fan, Z., Xu, W., Xiao, J., 2023a. Accelerating electrochemical CO_2 reduction to multi-carbon products via asymmetric intermediate binding at confined nanointerfaces. Nat. Commun. 14, 1298.
Zhang, L., Ge, L., Deng, L., Tu, X., 2022. Dual application: p-CuS/n-ZnS nanocomposite construction for high-efficiency colorimetric determination and photocatalytic degradation of tetracycline in water. Nanomaterials 12, 4123.
Zhang, X., Guo, S.-X., Gandionco, K.A., Bond, A.M., Zhang, J., 2020. Electrocatalytic carbon dioxide reduction: from fundamental principles to catalyst design. Mater. (Basel) Today Adv. 7, 100074.
Zhang, Z.-Y., Tian, H., Bian, L., Liu, S.-Z., Liu, Y., Wang, Z.-L., 2023b. Cu-Zn-based alloy/oxide interfaces for enhanced electroreduction of CO_2 to C2+ products. J. Energy Chem. (Easton) 83, 90–97.
Zhao, J., Deng, J., Han, J., Imhanria, S., Chen, K., Wang, W., 2020. Effective tunable syngas generation via CO_2 reduction reaction by non-precious Fe-NC electrocatalyst. Chem. Eng. J. 389, 124323.
Zhao, Z., Peng, X., Liu, X., Sun, X., Shi, J., Han, L., Li, G., Luo, J., 2017. Efficient and stable electroreduction of CO $_2$ to CH 4 on CuS nanosheet arrays. J. Mater. (Basel) Chem. (Easton) A 5, 20239–20243.
Zhen, J.-Z., Liu, J.-X., Chen, T.-Y., Shi, F., Dai, Y.-N., Yang, B., Li, Y.-F., Wang, X., Nong, T.-G., Hu, Y.-Q., 2019. Fabrication of ZnS/Zn electrode using sulphur infiltration method for CO2 reduction into CO in organic media. J. Alloys Compd. 771, 994–999.
Zhou, Y., Martín, A.J., Dattila, F., Xi, S., López, N., Pérez-ramírez, J., Yeo, B.S., 2022. Long-chain hydrocarbons by CO_2 electroreduction using polarized nickel catalysts. Nat. Catal. 5, 545–554.